Analytic Projection From Plane-Wave and PAW Wavefunctions and Application to Chemical-Bonding Analysis in Solids

Stefan Maintz,[a] Volker L. Deringer,[a] Andrei L. Tchougréeff,[a] and Richard Dronskowski*[a,b]

Quantum-chemical computations of solids benefit enormously from numerically efficient plane-wave (PW) basis sets, and together with the projector augmented-wave (PAW) method, the latter have risen to one of the predominant standards in computational solid-state sciences. Despite their advantages, plane waves lack local information, which makes the interpretation of local densities-of-states (DOS) difficult and precludes the direct use of atom-resolved chemical bonding indicators such as the crystal orbital overlap population (COOP) and the crystal orbital Hamilton population (COHP) techniques. Recently, a number of methods have been proposed to overcome this fundamental issue, built around the concept of basis-set projection onto a local auxiliary basis. In this work, we propose a novel computational technique toward this goal by transferring the PW/PAW wavefunctions to a properly chosen local basis using analytically derived expressions. In particular, we describe a general approach to project both PW and PAW eigenstates onto given custom orbitals, which we then exemplify at the hand of contracted multiple-ζ Slater-type orbitals. The validity of the method presented here is illustrated by applications to chemical textbook examples—diamond, gallium arsenide, the transition-metal titanium—as well as nanoscale allotropes of carbon: a nanotube and the C_{60} fullerene. Remarkably, the analytical approach not only recovers the total and projected electronic DOS with a high degree of confidence, but it also yields a realistic chemical-bonding picture in the framework of the projected COHP method. © 2013 Wiley Periodicals, Inc.

DOI: 10.1002/jcc.23424

Introduction

First-principles electronic-structure computations have become an invaluable part of today's solid-state chemistry, physics, and materials science. Among the most important frameworks for such approaches is the use of periodic plane-wave (PW) basis sets in combination with elaborated density-functional theory (DFT) parametrizations. The amenities of PW bases are computational efficiency,[1] the excellent compliance with structural optimization cycles,[2] the principal absence of basis-set bias or basis-set superposition errors,[3] and the ability to describe extended materials beyond "classical" densely packed solids: low-dimensionally extended structures such as graphene[4] or nanotubes,[5] surfaces and adsorbates,[6] isolated molecules[7] and crystalline fragments,[8] all in the same framework.

To analyze and interpret the complicated electronic structures of solid-state materials, chemical bonding concepts based on atomic orbitals (AOs) have turned out as especially profitable. Indeed, techniques such as the crystal orbital overlap population (COOP)[9,10] and the analogous crystal orbital Hamilton population (COHP)[11,12] provide a straightforward view onto orbital-pair interactions, and they have been used in a plethora of scientific contributions (for some recent applications see Ref. 13). However, by their very nature, these methods require a local description of the electronic structure in terms of atom-centered orbitals which then allow to construct the overlap and Hamilton operator matrices. In other words, both COOP and COHP are not directly accessible in any PW framework.

Fortunately enough, it is possible to regain the required locality by reconstructing the electronic wavefunction, that is, by projecting it onto a suitably chosen local auxiliary basis.[14–20] Several approaches toward this aim exist, and as early as in 1977, Chadi implemented a projection from delocalized wavefunctions to local orbitals.[14] We mention Sáchez-Portal, Artacho, and Soler,[15] who first projected PW eigenstates to different types of local basis sets,[16] thereby introducing the conceptual framework that, in principle, underlies the present work, too. Sánchez-Portal et al. showed how the reconstructed wavefunction can be analyzed to recover chemical information: band structures and also Mulliken population analyses for those obtained orbitals. Segall et al. took this method to project onto orbitals that were built from the pseudopotentials used for the PW calculation,[17] and applied traditional population analyses such as the Mulliken scheme to a range of bulk materials,[18] as well. A further advantage of such projection techniques was outlined by Bester and Fähnle who, by projecting plane waves onto a local basis in a mixed-basis framework, were able to use the "covalent energy" E_{cov} bonding indicator.[19] In a previous work,[21] we introduced a variant of

[a] *S. Maintz, V. L. Deringer, A. L. Tchougréeff, R. Dronskowski*
Institute of Inorganic Chemistry, RWTH Aachen University, Landoltweg 1, 52056 Aachen, Germany
E-mail: drons@HAL9000.ac.rwth-aachen.de
[b] *R. Dronskowski*
Jülich–Aachen Research Alliance (JARA-HPC), RWTH Aachen University, 52056 Aachen, Germany

the familiar COHP approach that, other than before, stems from a PW computation and was consequently dubbed "projected COHP" (pCOHP); we will return to this concept in a moment. Shortly after that, Dunnington and Schmidt have independently reported on a projection technique from projector augmented-wave (PAW) wavefunctions, taking the PAW method into account explicitly. The projection facilitated natural bond orbital analysis with Gaussian-type local basis sets, and they obtained highly descriptive results.[20] Subsequent to the work of the latter authors, very recently other methods were reported that also use projections.[22–24] Although performed on different routes and with different methodologies, the very basic chemical intention of all these approaches is similar, namely, to extract easily interpretable bonding information from PW based DFT. Clearly, this field of research is gaining increased attention, and for good reason.

Theory

So, let us formulate the problem at hand: we seek to extract informative quantities regarding chemical-bonding analysis. The most easily retrievable of those is the local density-of-states (LDOS) function

$$\mathrm{LDOS}_{\mu\vec{T},\mu'\vec{T}'}(E) = \sum_{j,\vec{k}} \mathrm{C}^{*}_{\mu\vec{T},j}(\vec{k})\mathrm{C}_{\mu'\vec{T}',j}(\vec{k})\delta(\varepsilon_j(\vec{k})-E), \qquad (1)$$

where $\boldsymbol{C}(\vec{k})$ contains the coefficients of linear combinations of AOs μ to represent crystal orbitals (LCAO-CO), building the wavefunction of the j-th band. The indices of the AOs are a short-hand notation ($\mu \equiv A, L$) to represent the orbital at atom A, positioned at the point $\vec{R}_A$ in the unit cell given by the lattice vector $\vec{T}$, with the quantum numbers L ($\equiv n$, l, and m). In all of the following, we separate the indices for rows and columns of matrix entries by a comma. Here is another matter of definition (or taste): in a true LCAO computation, we speak of an LDOS, whereas in a projected framework we speak of the projected DOS (pDOS); the above definition still holds, the only difference being the route to obtain the coefficient matrices $\boldsymbol{C}(\vec{k})$.

In passing, this very definition leads to the well-known COOP analysis, if one only looks at the so-called off-site elements in eq. (1), indexed by ν,

$$\mathrm{COOP}_{\mu\vec{T},\nu\vec{T}'}(E) = S_{\mu\vec{T},\nu\vec{T}'} \sum_{j,\vec{k}} C^{*}_{\mu\vec{T},j}(\vec{k})C_{\nu\vec{T}',j}(\vec{k})\delta(\varepsilon_j(\vec{k})-E), \qquad (2)$$

if μ and ν are centered on different atoms A and B. We note that the projected analog [which would be dubbed projected crystal orbital overlap population (pCOOP)] has in fact been applied already in 1998,[25] but has not gained too much attention since then, possibly due to a lack of broad availability.

The same framework leads to another definition, namely, the COHP; the latter may be energy-integrated to yield a measure of chemical-bonding strength and it was originally defined in 1993 as[11]

$$\mathrm{COHP}_{\mu\vec{T},\nu\vec{T}'}(E) = H_{\mu\vec{T},\nu\vec{T}'} \sum_{j,\vec{k}} f_j(\vec{k})C^{*}_{\mu\vec{T},j}(\vec{k})C_{\nu\vec{T}',j}(\vec{k})\delta(\varepsilon_j(\vec{k})-E). \qquad (3)$$

Here, $H_{\mu\vec{T},\nu\vec{T}'}$ are the elements of the Hamiltonian matrix $\boldsymbol{H}$, and $f_j(\vec{k})$ are the occupation numbers.* Its projected analog, the pCOHP, was introduced in our previous work[21] under the assumption that the projections—and by that the matrices $\boldsymbol{C}(\vec{k})$—are available. This work will deal with the projection itself and an analytically robust way to obtain these projections.

Where do we start?

As said before, the definitions of eqs. (1)–(3) are specified in a basis of local AOs of a solid and thus, their application is not directly possible in a PW-based framework. These equations also reveal that the key quantities are given in terms of the band (Bloch) states, written as an LCAO-CO. In contrast, a PW-based PAW calculation for a solid gives the band wavefunction $|\psi_j(\vec{k})\rangle$ expressed through a pseudospace (PS) function $|\tilde{\psi}_j(\vec{k})\rangle$ and an additional "augmentation part":[26]

$$|\psi_j(\vec{k})\rangle = |\tilde{\psi}_j(\vec{k})\rangle + \sum_{\mu\vec{T}} (|\phi_{\mu\vec{T}}\rangle - |\tilde{\phi}_{\mu\vec{T}}\rangle)\langle\tilde{p}_{\mu\vec{T}}|\tilde{\psi}_j(\vec{k})\rangle. \qquad (4)$$

Atomic calculations, performed during the generation of the PAW data set, yield appropriate all-electron (AE) partial waves $|\phi_\mu\rangle$ and the PS partial waves $|\tilde{\phi}_\mu\rangle$; both are then tabulated and stay unmodified during the actual quantum-chemical computation (and that is one of the aspects that make the method elegant). These quantities are defined within spheres around the atoms in the unit cell, and we find their periodic replicas in different unit cells (at the respective translation vector $\vec{T}$) using the phase factor $\exp\{i\vec{k}\vec{T}\}$. To make those PAW datasets more versatile, it is possible to use multiple orbitals to each l channel.[27] Those partial waves essentially define the projector functions $|\tilde{p}_{\mu\vec{T}}\rangle$, which are dual to the PS partial waves:

$$\langle\tilde{p}_{\mu\vec{T}}|\tilde{\phi}_{\nu\vec{T}'}\rangle = \delta_{\mu\nu}\delta_{\vec{T}\vec{T}'}. \qquad (5)$$

The quantity that is optimized during each PAW calculation is the PS wavefunction for the j-th band, and it is defined as an expansion over plane waves as in

$$|\tilde{\psi}_j(\vec{k})\rangle = \frac{1}{\sqrt{\Omega}} \sum_{\vec{G}} C^{\mathrm{PW}}_{j\vec{G}}(\vec{k})e^{i(\vec{k}+\vec{G})\vec{r}}, \qquad (6)$$

where Ω is the volume of the unit cell in real space, and the sum runs over reciprocal-space vectors $\vec{G}$—infinitely many, in theory; sufficiently many to achieve reasonable convergence, in practice.

*Note that the occupation numbers given in the COHP definition would render any visualization above the Fermi level zero. Thus, for drawing $-\mathrm{COHP}(E)$ plots, these occupation numbers are omitted by convention.

Projection: the central idea

To establish correspondence between the PAW and LCAO-CO settings, we request that the PAW band functions coincide with the projected band functions $|\mathcal{X}_j(\vec{k})\rangle$;[22] the latter are given by the expansions over all basis AOs, again indexed by ν:

$$|\psi_j(\vec{k})\rangle \stackrel{!}{=} |\mathcal{X}_j(\vec{k})\rangle \;=\; \sum_{\nu\vec{T}} C_{\nu\vec{T},j}(\vec{k})|\chi_{\nu\vec{T}}\rangle. \tag{7}$$

In contrast to our previous work—which served as a methodological proof of concept and introduced the pCOHP as such—we now search for a full, analytic projection formalism that takes into account the peculiarities of the PW/PAW method, as well. The derivation given here is hence somewhat lengthy and many of the presented formulas have already been given elsewhere, but we believe it will be useful to have exact expressions in a self-consistent form at hand at this stage. We also note that the theory presented in Ref. 21 is straightforwardly generalized and in this way made applicable to a wide range of complex solid-state systems.

Equation (7) manifests once more that the crucial step to accomplish is finding the LCAO-CO coefficients—here, collected in the $\boldsymbol{C}(\vec{k})$ matrix—from the results of a self-consistent PAW computation. In order to do so, we combine the AOs to the Bloch sums[28] corresponding to a specific value of $\vec{k}$:

$$|\chi_\mu(\vec{k})\rangle = \frac{1}{\sqrt{N_{\vec{T}}}}\sum_{\vec{T}} e^{i\vec{k}\vec{T}}|\chi_{\mu\vec{T}}\rangle. \tag{8}$$

Then, we multiply this into eq. (7) from the left, thereby yielding expansion coefficients of $|\mathcal{X}_j(\vec{k})\rangle$ in terms of the Bloch sums $B_{\mu,j}(\vec{k})$

$$\langle\chi_\nu(\vec{k})|\mathcal{X}_j(\vec{k})\rangle = \sum_\mu \underbrace{\langle\chi_\nu(\vec{k})|\chi_\mu(\vec{k})\rangle}_{=S_{\mu,\nu}(\vec{k})} B_{\mu,j}(\vec{k}), \tag{9}$$

and these expansion coefficients are connected to $\boldsymbol{C}(\vec{k})$ via

$$C_{\mu\vec{T},j}(\vec{k}) = \frac{1}{\sqrt{N_{\vec{T}}}} e^{i\vec{k}\vec{T}} B_{\mu,j}(\vec{k}). \tag{10}$$

In our previous work,[21] the overlap between the PW-based wavefunction and a local orbital was dubbed transfer-matrix element $T_{\mu,j}(\vec{k})$. Combining this with eqs. (7) and (9), we obtain

$$T_{\mu,j}(\vec{k}) = \langle\chi_\mu(\vec{k})|\psi_j(\vec{k})\rangle \stackrel{(7)}{=} \langle\chi_\mu(\vec{k})|\mathcal{X}_j(\vec{k})\rangle \tag{11}$$

$$\stackrel{(9)}{=} \sum_\nu S_{\mu,\nu}(\vec{k})B_{\nu,j}(\vec{k}) \tag{12}$$

or, in terms of matrix algebra,

$$\boldsymbol{S}(\vec{k})\boldsymbol{B}(\vec{k}) = \boldsymbol{T}(\vec{k}). \tag{13}$$

This equation system can be solved for $\boldsymbol{B}(\vec{k})$ using the LU (lower/upper triangular matrix) or singular value decompositions (SVD) of $\boldsymbol{S}(\vec{k})$.

As eq. (13) shows, $\boldsymbol{B}(\vec{k})$ is derived from $\boldsymbol{T}(\vec{k})$, and the latter is needed. Within the PAW framework, two representations of the wavefunctions—AE and PS—are given. Here, we stick to the AE representation; starting from eq. (4) and introducing the short-hand notation $|\tilde{\phi}_\mu\rangle \equiv |\phi_\mu\rangle - |\tilde{\phi}_\mu\rangle$, we get

$$T_{\mu,j}(\vec{k}) = \underbrace{\langle\chi_\mu(\vec{k})|\tilde{\psi}_j(\vec{k})\rangle}_{=T^{\mathrm{PS}}_{\mu,j}(\vec{k})} + \underbrace{\sum_{\mu\vec{T}}\langle\chi_\mu(\vec{k})|\tilde{\phi}_{\mu\vec{T}}\rangle\langle\tilde{p}_{\mu\vec{T}}|\tilde{\psi}_j(\vec{k})\rangle}_{=T^{\mathrm{aug}}_{\mu,j}(\vec{k})}. \tag{14}$$

Hence, the transfer-matrix element (from which everything else will then be derived) has been separated into two additive parts—first, the projection of the PS wavefunction onto local orbitals, $T^{\mathrm{PS}}_{\mu,j}(\vec{k})$, and second, the projection of the augmentation part, $T^{\mathrm{aug}}_{\mu,j}(\vec{k})$. As seen in the above equation, we are left with three scalar products (or specific to function space: integrals) to evaluate.

Three scalar products

First, we deal with $T^{\mathrm{PS}}_{\mu,j}(\vec{k})$ analytically. The rigorous derivation is given in the Appendix for clarity. Using another convenient short-hand notation, $\kappa \equiv k + G$, we need to search for

$$T^{\mathrm{PS}}_{\mu,j}(\vec{k}) = \sqrt{\frac{N_{\vec{T}}}{\Omega}}\sum_{\vec{G}} C^{\mathrm{PW}}_{j\vec{G}}(\vec{k})e^{i\vec{\kappa}\vec{R}_A}\int \mathrm{d}^3\vec{r}\, e^{i\vec{\kappa}\vec{r}}\chi^*_\mu(\vec{r}). \tag{15}$$

For obvious reasons, local atom-centered orbitals are routinely defined as having real, not complex radial parts; this is true also for the Slater-type orbitals (STOs) we seek to use here. Furthermore, for reasons of chemical interpretability,[13] we also choose real spherical harmonics to reflect the topology of the local orbitals (i.e., we use p_x, p_y orbitals and so on). This makes $\chi_\mu(\vec{r})$ real-valued, as well, and the complex conjugate in eq. (15) may be dropped. In addition, the reciprocal lattice vectors $\vec{G}$ are chosen such that their scalar products with the real-space translation vectors simplify to $\vec{G}\cdot\vec{T} = 2\pi$, as is done in standard PAW codes.

Mathematically, the remaining integral term of eq. (15) is a Fourier transformation (FT) of the local orbital $\chi_\mu(\vec{r})$, which we will denote as $\hat{\chi}_\mu(\vec{\kappa}) = \int d^3\vec{r}\; e^{i\vec{\kappa}\cdot\vec{r}}\chi_\mu(\vec{r})$, and we will return to the choice of $\hat{\chi}_\mu$ in a moment. Inserting it into eq. (15) yields an analytic formula to calculate the PS transfer-matrix elements given that the FT of the AO is known:

$$T^{\mathrm{PS}}_{\mu,j}(\vec{k}) = \sqrt{\frac{N_{\vec{T}}}{\Omega}}\sum_{\vec{G}} C^{\mathrm{PW}}_{j\vec{G}}(\vec{k})e^{i\vec{\kappa}\cdot\vec{R}_A}\hat{\chi}_\mu(\vec{\kappa}). \tag{16}$$

If one used a true PW code, that is, did not make use of the PAW method, this integral would constitute the entire transfer matrix $\boldsymbol{T}(\vec{k})$. In practice, however, doing so is not very much worthwhile because in proximity to the atomic cores, the wavefunctions oscillate strongly, which would require enormous amounts of PWs to describe. The PAW method reduces the necessary number of PWs dramatically.[26,27] Within the PAW framework, however, neither the PS nor the

augmentation part can be interpreted alone, as the PAW transformation is not norm-conserving.

Incidentally, eq. (16) gives the recipe to calculate the third scalar product in eq. (14), $\langle \tilde{p}_\mu | \tilde{\psi}_j(\vec{k}) \rangle$, just as well. The FT of the projector functions p_μ is either known and directly tabulated in the PAW data set, or it can be easily obtained via a Fourier–Bessel transformation; hence, one may simply replace $\hat{\chi}_\mu(\vec{\kappa})$ with $\tilde{p}_\mu(\vec{\kappa})$ in eq. (16), yielding the next required scalar product.

This leaves us with one final expression—that which takes care of the difference between the AE and PS partial waves $|\bar{\phi}_i\rangle$, again derived in the Appendix:

$$\langle \chi_\mu | \bar{\phi}_\mu \rangle = \delta_{ll'} \delta_{mm'} \int_0^{r_c} dr \chi_\mu^*(r) \bar{\phi}_\mu(r). \tag{17}$$

The integration boundaries range from the center of the PAW sphere (where $r = 0$) up to r_c, that is, the radius after which the AE and PS partial waves coincide. There, the difference function $|\bar{\phi}_i\rangle$ and hence the integrand fall to zero.

Choosing a local basis

At this point, only one step is left to obtain the coefficient matrix $\boldsymbol{B}(\vec{k})$: one needs to choose local orbitals and transform them to reciprocal space. In this work, we use the functions given by Bunge, Barrientos, and Bunge.[29]† In principle, however, the choice of basis is arbitrary, as long as the latter is able to represent the PAW function and allows for chemical interpretation. The basis set used here is minimal and contracted from multiple primitive STOs, and so we first need an FT formulation of STOs. Fortunately, more than two decades ago already, Belkič and Taylor[32] derived a unified formula for STOs in reciprocal space using the Gegenbauer polynomial. For conciseness, we do not repeat their result but note that the FT normalization constant of $(2\pi)^{-3}$ (which is a matter of definitions) must be excluded from eq. (21) of Ref. 32 in our case.

The pDOS and pCOOP as given in eqs. (1) and (2) are now available. To finally carry out energy-resolved pCOHP analyses, conversely, we still lack the Hamiltonian matrix in terms of LCAOCOs as extracted from the PAW function. Previously,[21] we have retrieved the projected Hamiltonian matrix $\boldsymbol{H}^{(\mathrm{proj})}(\vec{k})$ via

$$H_{\mu,\nu}^{(\mathrm{proj})}(\vec{k}) = \sum_j T_{\mu,j}^*(\vec{k})\, \varepsilon_j(\vec{k})\, T_{\nu,j}(\vec{k}), \tag{18}$$

but in this work, we use a basis that is not orthogonal anymore and, accordingly, does violate the constraints of eq. (18). Thus, a new way to regain $\boldsymbol{H}^{(\mathrm{proj})}(\vec{k})$ in the more general case of nonorthogonal bases must be sought.

†The basis set given in Ref. 29 is tabulated from He to Xe (and the STO description of H is trivial, of course). If heavier atoms are to be analyzed, we refer to the works in Refs. 30 and 31. In fact, we have tested this basis set as well, which gave results indistinguishable from those reported here. Koga et al., however, used a larger number of primitive basis functions, which increases computational effort, so we stick to the smaller basis given in Ref. 29 where possible.

Reconstructing the *H* matrix

Reminiscent of the Roothaan–Hall equations, the Kohn–Sham Hamiltonian matrix $\boldsymbol{H}_{\mathrm{KS}}(\vec{k})$ and the coefficient matrix $\boldsymbol{C}(\vec{k})$ are generally connected by

$$\boldsymbol{H}_{\mathrm{KS}}(\vec{k})\boldsymbol{C}(\vec{k}) = \boldsymbol{O}(\vec{k})\boldsymbol{C}(\vec{k})\boldsymbol{\varepsilon}(\vec{k}), \tag{19}$$

where $\boldsymbol{\varepsilon}(\vec{k})$ is a diagonal matrix containing the electronic eigenvalues and $\boldsymbol{O}(\vec{k})$ is the overlap matrix of the band wavefunctions $O_{j,j'}(\vec{k}) = \langle \mathcal{X}_j(\vec{k}) | \mathcal{X}_{j'}(\vec{k}) \rangle$ which, in terms of the (adjoint) coefficient matrix $\boldsymbol{C}^*(\vec{k})$, is

$$\boldsymbol{O}(\vec{k}) = \boldsymbol{C}^*(\vec{k})\boldsymbol{S}(\vec{k})\boldsymbol{C}(\vec{k}). \tag{20}$$

If we assume an ideal projection, the reconstructed band wavefunctions $|\mathcal{X}_j(\vec{k})\rangle$ as built from the columns of the coefficient matrix $\boldsymbol{C}(\vec{k})$ are, in fact, orthonormal to each other, because the original PW/PAW wavefunctions must be. In this case, the overlap matrix in eq. (19) equals unity and can be dropped.

In any case, we require that the crystal wavefunction consists of at least as many band wavefunctions as there are functions in the local basis. Thus, the equation system $\boldsymbol{H}_{\mathrm{KS}}(\vec{k})\boldsymbol{C}(\vec{k}) = \boldsymbol{C}(\vec{k})\boldsymbol{\varepsilon}(\vec{k})$ becomes (over)determined, and after applying transposition identities, the Kohn–Sham Hamiltonian can be retrieved using standard linear equation system solvers [cf. eq. (13)]. Inserting the result into eq. (3), pCOHP analysis is finally enabled in the new analytical framework.

Technical Aspects

Until now, we have dealt with an ideal theory, but when transferring it into numerical practice other challenges arise. With eqs. (13), (16), and the choice of a local basis,[29,32] we have retrieved the linear combination coefficients to further investigate the properties of $|\mathcal{X}_j(\vec{k})\rangle$. The fundamentals of quantum mechanics postulate that band wavefunctions are orthonormal, and we notice that the PAW band functions $|\psi_j(\vec{k})\rangle$ fulfill this requirement. By projecting onto a finite basis of AOs (or their Bloch sums), however, it is very well possible that the resulting projected band functions are not orthonormal. This is easily understood by looking at the norm of a projected wavefunction that differs from unity if the local AO basis does not fully cover the entire Hilbert space. As a consequence, essential information is lost, and it is crucial to quantify its amount in order to justify a reasonable projection. On that route, the so-called "spilling parameter" as introduced by Sánchez-Portal, Artacho, and Soler[16] is easily understood, which in the notation of this work reads

$$\mathcal{S}_\Omega = \frac{1}{N_k N_j} \sum_k \sum_j \left(1 - O_{jj}(\vec{k})\right) f_j(\vec{k}), \tag{21}$$

with $0 \leq \mathcal{S}_\Omega \leq 1$; zero indicates an ideal projection. In practice, the projected function will deviate from the original one, which generally destroys normalization and hence violates the previously mentioned orthonormality condition. Thus, the

projected band wavefunctions need to be orthonormalized. Multiple methods are known to do so; here, we chose Löwdin's symmetric orthonormalization procedure as it keeps the functions as close to their originals as possible,[33] which perfectly fits the needs of a projection.‡ To apply Löwdin's orthonormalization and simultaneously avoid numerical instabilities arising in the calculation of the inverted overlap matrix, we seek for $\boldsymbol{O}^{\frac{1}{2}}(\vec{k})$ via SVD and solve for a new set of coefficients $\boldsymbol{C}^{\perp}(\vec{k})$ to represent the desired orthonormalized projected band wavefunctions as given in

$$\boldsymbol{C}^{\perp}(\vec{k})\boldsymbol{O}^{\frac{1}{2}}(\vec{k}) = \boldsymbol{C}(\vec{k}). \tag{22}$$

In practice, we have to add another formal caveat to the otherwise analytical framework presented here. Although the STOs are analytically defined, the partial waves $|\bar{\phi}_i(r)\rangle$ are, in computational practice, tabulated as pseudopotential parameters used by the quantum-mechanical code. In this case, the scalar product $\langle\chi_\mu|\bar{\phi}_\mu\rangle$ as given in eq. (17) is conveniently computed by numerical quadrature on the given real-space grids, making use of interpolation routines to yield reasonably precise results. A full analytic derivation would of course be thinkable as well, if one had the analytic expressions for $|\phi_\mu\rangle$ and $|\tilde{\phi}_\mu\rangle$ available. For our purpose, the numerical integration is perfectly viable.

All the aforementioned projection and analytic methods have been implemented in a standalone computer program which processes PAW parameters and self-consistent results from the Vienna *ab initio* Simulation Package (VASP);[2,34,35] we used the latter in revision 5.2.12, together with the Perdew–Burke–Ernzerhof-generalized gradient approximation (PBE-GGA) exchange–correlation functional[36] and Gaussian smearing or tetrahedron integration[37,38] over $\vec{k}$ points chosen after Monkhorst and Pack.[39]§ All DOS, pCOOP, COHP, and pCOHP plots were generated using the wxDragon visualization software.[40] Unless mentioned otherwise, default parameters have been used for the self-consistent computations and all of them refer to energetically optimized atomic structures. For comparison with traditional tools, the electronic structures were recalculated using TB-LMTO-ASA theory,[41,42] using the Perdew–Wang semilocal correction[43] in addition to the Vosko–Wilk–Nusair local functional.[44]

It should nonetheless be noted that our methods are principally independent of the particular PW electronic-structure code, as reading the PS wavefunction and PAW data is merely a technical task; the chemistry happens before (in the self-consistent computation) and afterward (in the projection and bonding analysis). Also, the format of the wavefunctions does not depend on the particularities of the computation such as choice of exchange–correlation functional; the chemistry may well do so, but this is left to the discretion of the user. In short, any suitable PW/PAW code (or even compatibly implemented methods like ultrasoft pseudopotentials) may in principle be used for analyses as they are described here.

‡The alert reader will have noticed that due to reorthonormalization, higher lying states might get mixed into the occupied states and, strictly speaking, the direct equivalence between PAW and the projected states would be lost. And yet, the off-diagonal entries of the Löwdin matrix (which mathematically account for the described mixing) were checked to be smaller than 0.025 in all of the presented examples and, thus, it is assured that the results are reasonable.

§Our preliminary implementation does not yet cover space-group symmetry. In other words, some of our test cases required a *k* point mesh generated on the complete Brillouin zone (not only the irreducible wedge) at the present time. In the future, space-group symmetry may of course be implemented to save computing resources.

Applications

Diamond

As a first example, we address a classical test case which has already been the subject of our previous work:[21] carbon in its diamond allotrope. Ahead of pCOHP analysis, we need to verify how well our projection can recover the electronic states. We stress that we use a minimal valence-only basis, that is, the C 1s orbital is omitted but for a good reason: it has virtually no contribution in the energetic window under study. Following eq. (21), our method reaches $\mathcal{S}_Q = 7.97\%$ such that it spills nearly 8% of the spectral density of the occupied subspace. This relatively large value may be explainable by the fact that the PAW spheres do overlap by 0.04 Å in this particular case, rendering the assumptions around eq. (A8) in the Appendix less than ideal. Indeed, if hard PAW potentials for carbon are used (i.e., $|\bar{\phi}_{\mu\vec{r}}\rangle$ is more contracted), the spheres become well separated by 0.35 Å, and the charge spillage is reduced to 1.05%, thereby supporting the aforementioned assumption. Furthermore, it is very well possible to improve the local basis for this element. We note, however, that all results based on the hard potentials led to pDOS, pCOOP, and pCOHP curves that are virtually superimposable with those based on the standard potentials, and this is why we stick to the latter in the following. Apparently, the particular methods applied here for chemical-bonding analysis are quite insensitive even when noticeable spilling occurs.

For facile visual interpretation, we start our evaluation by computing the orbital-projected DOS and summing it up over all orbitals (C 2s, 2p) and atoms in the unit cell. Using eq. (1), the pDOS is easily accessible, and we require that the sum of local s- and p-projections gets reasonably close to the total DOS curve. Recall that in methods such as TB-LMTO-ASA,[41,42] the atomic contributions intrinsically sum up to give the total DOS but in PW DFT this is generally not the case, not by fault of the electronic-structure codes or their creators but due to the PW nature itself, and this issue has been discussed recently.[45]

In Figure 1, two methods to compute the pDOS are visualized, and the results are shown alongside the corresponding total DOS. Comparing the results of the pDOS calculated in the conventional manner, namely by projecting onto PAW spheres as given by default program output (hereafter called "spherical projection"), our method not only surpasses the spherical projection, but also nearly coincides with the total DOS, at least visually, which is a direct consequence of the matrices leading to the pDOS curves having been reorthonormalized; given a successful projection they must trivially yield

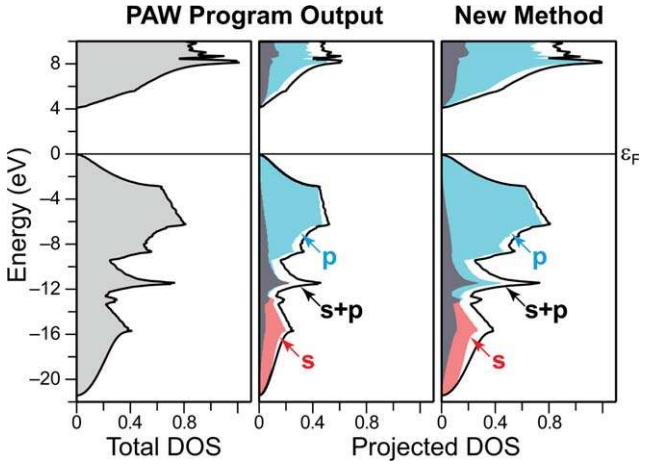

Figure 1. Left: Total electronic DOS for diamond computed using VASP. Middle: Orbital-pDOS as obtained from default routines of the PW/PAW program. Carbon s and p contributions are indicated by red and cyan shading, respectively. The sum of both is given by a solid line. Right: As before but, this time, obtained from the analytical projection scheme we describe here. In all plots, the energy zero is chosen to coincide with the Fermi level ε_F.

the correct number of electrons in total, let for numerical deviations. Note that this does not guarantee a correct distribution of the electrons over the various *l* channels; here, we will probe the assignment to the carbon s- and p-levels.

So, let us compare the sum of the integrated pDOS to the integrated total DOS. The latter equals exactly eight electrons, trivially so because two carbon atoms contribute $2\times4=8$ valence electrons, whereas the spherical projection yields only 5.11 electrons, losing about 36% of the spectral density. In contrast, 7.99993 electrons are recovered by the analytical technique of which 2×1.1 electrons are attributed to each s-state and 2×2.9 electrons belong to p-states. This is in full agreement with the expectations.

Let us move on and apply those bond-analytic tools we have mentioned at the beginning of this article. In Figure 2,

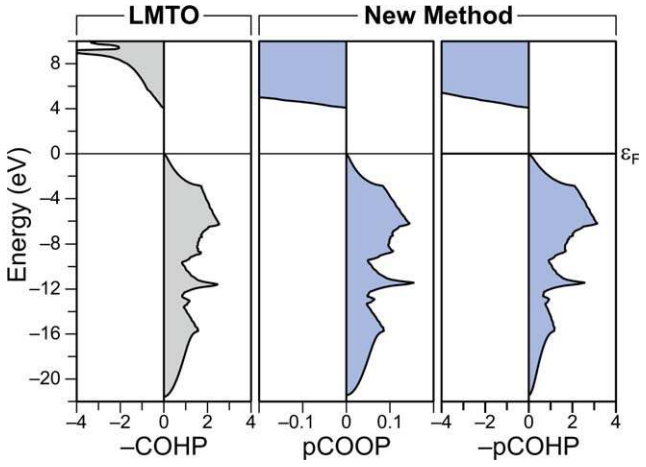

Figure 2. Chemical-bonding analysis for the C—C bond in diamond. Left: Traditional COHP analysis performed by the TB-LMTO-ASA program. Right: pCOOP and Hamilton populations (pCOHP), obtained with the new PW/PAW-based method. As is convention, all plots show bonding (stabilizing) contributions to the right of the vertical line, and antibonding (destabilizing) contributions to the left.

the result of the COHP analysis carried out within the traditional LMTO framework has been plotted to allow for a comparison with the new method. All approaches shown, similar in thought but different in technique, are in very good agreement; all of them correctly identify the entire valence region as bonding which is evidenced by positive −COHP and −pCOHP contributions.[13] The electronic situation is perfectly optimized and any electronic density hypothetically added would push the Fermi level ε_F up into the antibonding area ($-$(p)COHP < 0), thereby destabilizing the crystal. It is also convenient that the pCOOP gives qualitatively the same result.

Gallium arsenide

As a second example, we move to another case already looked at in our previous work:[21] the semiconductor gallium arsenide (GaAs), structurally related to diamond, which is a similar problem yet of slightly higher complexity.

Even though the PAW spheres overlap by 0.02 Å using standard potentials, the charge spilling arrives at a remarkably small value of $\mathcal{S}_Q = 0.04\%$ before orthonormalization. Apparently, the theoretical assumptions are very reasonable and the projection onto a minimal, valence-only basis is clearly sufficient in this case.

Again, we compare the sum of the pDOS with the total DOS in Figure 3. The latter gives exactly eight electrons as Ga and As contribute $3+5=8$ valence electrons, of which the spherical projection recovers only 5.0 electrons. The present method attributes 2.8 electrons to Ga states and 5.2 electrons to As which sums up to a total of 7.998 electrons (see the above comment regarding orthonormalization).

Let us look at the chemical bonding. As seen in Figure 4, the pCOHP analysis of the covalent Ga—As bond gives a result that, again, is qualitatively in full agreement with the expectations. Comparing the pCOHP with the LMTO result, the bonding contribution arising from the s-levels in the energetic window between −12 and −10 eV appears slightly underestimated in comparison to the LMTO reference. In contrast to

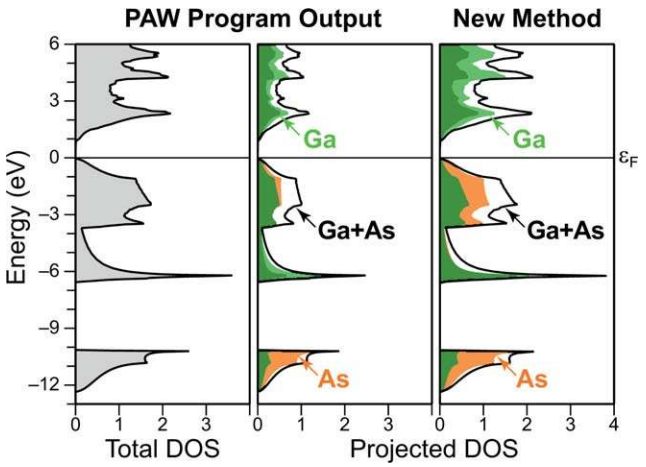

Figure 3. As Figure 1, but for crystalline gallium arsenide. Ga and As projections are indicated by green and orange shading, respectively. [Color figure can be viewed in the online issue, which is available at wileyonlinelibrary.com.]

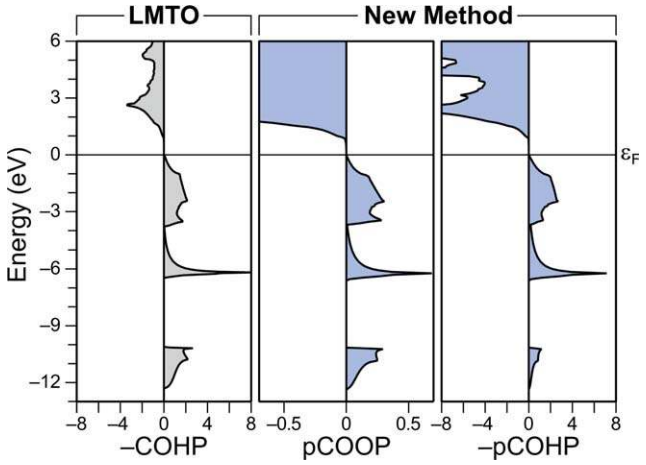

Figure 4. As Figure 2, but for the Ga—As bond in crystalline gallium arsenide. [Color figure can be viewed in the online issue, which is available at wileyonlinelibrary.com.]

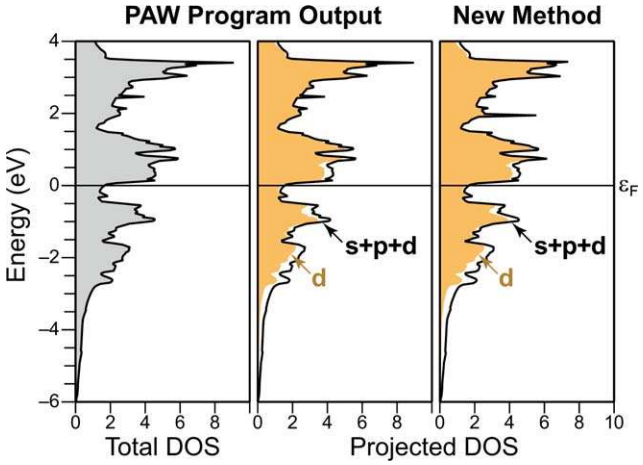

Figure 5. As Figure 1, but for hexagonal close-packed titanium. Projections onto Ti 3d (which make up the vast majority of the region near ε_F) are indicated by orange shading; the sums of s, p, and d projections are shown by solid lines. [Color figure can be viewed in the online issue, which is available at wileyonlinelibrary.com.]

our previous work,[21] the region between −4 eV and the Fermi level is now correctly reported as an unambiguously bonding contribution, presumably due to the improved projection technique. So, the magnitude of the $-\mathrm{COHP}(E)$ value shown on the horizontal axes is comparable which allows to put even more confidence into the reconstructed pCOHP result. Above the Fermi level ε_F (i.e., above the chosen energy zero in the figure), nonetheless, we encounter an overweighted (compared to LMTO theory) antibonding region above the Fermi level. The reason for the observed behavior can be easily understood if one realizes that the AO basis used in the present article is not defined for the empty atomic states, for example, the Rydberg ones. Nonetheless, whatever kind of projection of the empty bands is not a problem at all for bonding analysis, as the integrated quantities of interest include the occupation numbers which, of course, are zero in the region under discussion. There are no electrons above ε_F (at zero Kelvin).

Noticing that the TB-LMTO-ASA results are obtained on an entirely different theoretical footing, we conclude that the observed differences are not a fault of either method, but can be attributed to their very diverse natures. In fact, there is no fault at all, as long as both methods lead to the correct chemical conclusions. In this work, we look at the topology of the wavefunctions as reflected in the shape of the COHP and pCOHP curves, and the chemical-bonding nature is perfectly captured by either choice. In the future, one might certainly wish to improve the local auxiliary basis sets beyond the current minimal implementation, to be able to look at subtle energy differences in the integrated COHP and pCOHP, as well.

Titanium

As the next example of chemical-bonding analysis, we have chosen a somewhat more challenging one: titanium, a typical 3d metal.

As we see in Figure 5, the default spherical projection routine performs remarkably well in this case and yields a pDOS plot that, using the naked eye, is almost indistinguishable from our result. A possible reason is that about 70% of the electronic states in this region are of d-topology; those 3d orbitals, much more strongly contracted than 4s- or 4p-orbitals, are quite likely to be found within the integration sphere used for the projection.

Using a *k* point grid of 9×9×5 points without simplifications by space-group symmetry (see footnote, §), our method recovers 7.967 electrons in the summed pDOS. Of those electrons, 1.8 are attributed to s-levels, 0.7 to p-levels, and 5.6 to d-levels. As the credibility of the projection must be validated before orthonormalization, we again calculate the charge spilling which arrives at a very low value of $\mathcal{S}_Q = 0.12\%$.

Let us now look at the bonding nature of Ti. The hexagonal structure, as visualized in Figure 6a, contains two slightly different bond lengths (because Ti is almost, but not perfectly closest-packed) of which only the shorter bond (2.86 Å) is completely enclosed within the unit cell we have chosen. For reasons of simplicity, we will discuss only this shortest and strongest bond in the following.

The pCOHP of the Ti—Ti bond, given in Figure 6b on the right, is in remarkable agreement with the reference COHP calculated with LMTO on the left; qualitatively, both curves yield exactly the same interpretation of chemical bonding in elemental Ti. There are bonding states up to and above the Fermi level ε_F; assuming a rigid band model,[46] the electronic band structure is able to accommodate more electrons (which is exactly what happens upon moving to the right within the 3d-row of the periodic table), at least up to a certain point. If the Fermi level is shifted upward to the region where the (p)COHP intersects the vertical axis and thereby changes to antibonding character, however, the ensuing electronic instability induces magnetism, which reduces the occupation of antibonding states as analyzed in detail before.[46]

Nonetheless, very close examination of both functions reveals small differences. According to Figure 5, the energetic region from −6 to −4 eV contains a noticeable share of s-

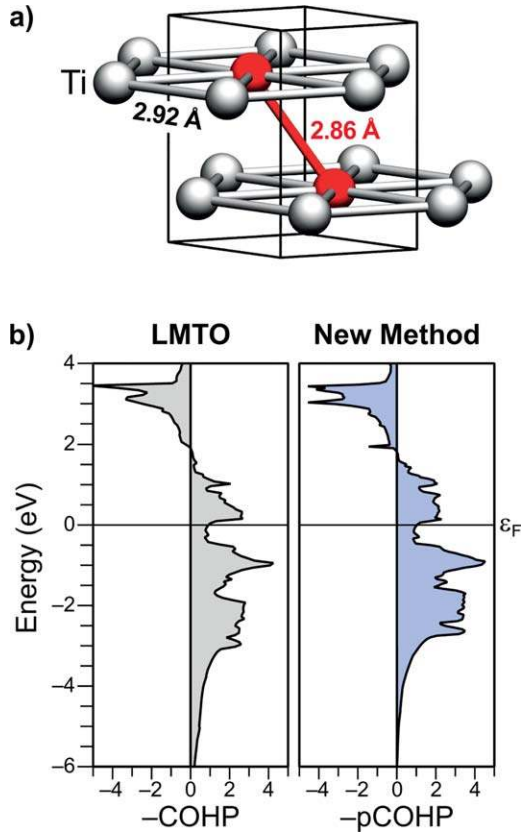

Figure 6. (a) Unit cell of hcp titanium (atoms inside the cell highlighted in red) and the second-nearest-neighbor coordination environment (gray). Note the two slightly different bond lengths. (b) COHP and pCOHP analysis as in Figure 2 for the nearest-neighbor Ti—Ti bond also shown in red. [Color figure can be viewed in the online issue, which is available at wileyonlinelibrary.com.]

and p-contributions. This very region is ascribed a stronger bonding character in the COHP (LMTO) than in the pCOHP (PW/PAW) framework. Acclaimed by our method, conversely, the d-state-dominated region in the direct vicinity of ε_F constitutes a stronger part in the Ti—Ti-bond.

What is the cause of these minor deviations? Apart from the different quantum-theoretical approaches, there is another aspect to be considered: to carry out pCOHP analysis, the theory formally requires that the number of bands included in the PAW calculation equals the number of local basis functions used to project upon [see eq. (19)]. Within our minimal valence basis, Ti in hexagonally closest packing gives 18 local basis functions (3×3p, 1×4s, and 5×3d functions for each of the two atoms in the unit cell). Of course, one may include 18 bands in the PAW computation (and this is exactly what we did), however, averaged over all *k* points only four of those 18 bands are occupied. It is doubtful that the employed minimal basis is able to fully reproduce the higher-lying, virtual bands, as there, naturally, functions with higher nodality (such as the mostly unoccupied 4p orbitals) would be required in the local basis. An overall (i.e., including the virtual bands) spilling parameter of $\mathcal{S}_\Omega = 11.72\%$ underlines this argument, but we stress again that the important part of COHP interpretation does not take place in regions high above the Fermi level and that energy integration would omit everything above ε_F completely. Nonetheless, multiple possibilities to improve the local auxiliary basis open up here, but these are subject to further research. In this work, we deliberately stick to a minimal and unoptimized STO basis—without orbitals unoccupied in the atomic ground states—to demonstrate its potential and limitations.

Beyond densely packed solids: a carbon nanotube

Until now, we have compared our results to the traditional COHP framework, namely, the well-established tight-binding LMTO-ASA code. In return—the reader may ask—are there systems which the latter cannot handle? There is an extremely important class of scenarios, namely, those that include artificial vacuum spacing. This is what is routinely used for PW/PAW simulation of nanoscale materials, countless times each day.

Of course, there are programs that do use local orbitals as their basis in the first place—take the popular CRYSTAL[47] and SIESTA[48] packages as two examples. Therein, no auxiliary projection is necessary and, in fact, COHP analysis has been implemented into SIESTA and was used successfully many times. We stress here that we do not want to challenge the merit of these programs, or join a pros and cons debate on plane waves. Instead, the goal of this article is to provide local analysis for PW/PAW codes, and we believe there is good reason to do so. As one example, Choi et al. used VASP for their simulations and then SIESTA, in a second step, to carry out COHP analyses.[49]

That being said, we turn to our next example: a carbon nanotube. Let us first model the system at hand: an isolated nanostructure (in contrast to the ideal crystals we handled so far) is translationally invariant only for one dimension, namely the one along the axis around which the surface of the tube is extended. Consequently, in the PW/PAW framework used, the model system needs to include sufficient vacuum perpendicular to the tube axis, so that the adjacent, replicated tubes do not noticeably interact with the original one.

Being bound to periodic boundary conditions as well, the reference COHP code TB-LMTO-ASA would require the use of so-called empty spheres—far too many to expect reasonable results. Thus, we are left with chemical intuition to rationalize the bonding situation of the nanotube. Naïvely, it can be regarded as a graphite layer which, however, is wrapped and glued together to form a tube. Fashionability of nanostructures aside, a chemist would expect its bonding nature to be rather close to graphite: the larger the radius of the tube, the closer the properties of the material become to graphite as the bending distortion decreases.[5] In Figure 7a, we show a COHP curve we have calculated for graphite, which is of course easily accessible with LMTO or any suitable DFT code.

In Figure 7b, we illustrate the structure and the chosen unit cell for the exemplary carbon nanotube system. In the self-consistent PAW computation and the subsequent projection, we used 35 *k* points along the tube axis in the Brillouin zone (again disregarding symmetry) and switched to Gaussian smearing integration with $\sigma = 0.2$ eV as used per default in

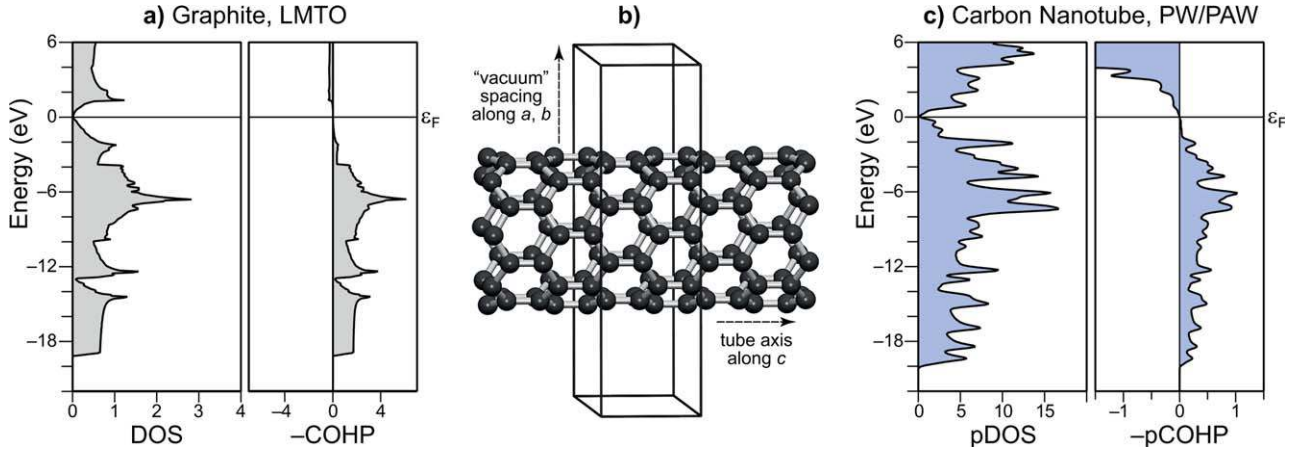

Figure 7. (a) DOS and COHP analysis for graphite as obtained with the traditional TB-LMTO-ASA approach. (b) PW supercell setup that models a carbon nanotube as used in this study. The boundaries of the simulation box are indicated; some atoms outside this unit cell have been added to improve visualization. (c) pDOS and pCOHP analysis for this system; the pCOHP curves have been averaged over all C—C bonds inside the unit cell. [Color figure can be viewed in the online issue, which is available at wileyonlinelibrary.com.]

VASP. This *k* point grid appeared as converged as even doubling its size led to indistinguishable results in the electronic DOS. The charge spilling of $\mathcal{S}_Q = 8.76\%$ is comparable to the value retrieved for diamond, which is subject to the same effects already discussed above; clearly, the amount of spilling is determined mainly by the atomic species and its PAW potentials, to a lesser extent by the particular allotrope studied.

Comparing the DOS and COHP results for graphite in Figure 7a to the results computed with our new method in Figure 7c, the first obvious difference is the relative smoothness of the LMTO quantities in comparison to the "spikes" in the PAW-based DOS and subsequently pCOHP. Such discretization, however, stems from the finite diameter of the tube (which is ascertained by the previously shown convergence with respect to the *k*-point grid size), not by whatever kind of computational artifact.

With respect to chemical-bonding analysis, graphite is the archetype for "sp^2" hybridized, quasi-two-dimensionally extended structures. The rectangular-like part in the region between −19 to −12 eV can be viewed as a fingerprint for such systems, as pointed out by Hoffmann.[50] The nanotube seems to have lost parts of this rectangular component in the projected quantities, but such effects are to be studied more thoroughly in the future.

Note also that the axis scaling of the pCOHP plot for the PAW case appears unexpectedly small. This is naturally due to a (symmetry-related) necessary averaging over all 48 bonds in the unit cell, that is, panel c) is given in pCOHP/bond whereas a) is given in COHP/cell.

An interesting characteristic that graphite and the nanotube seem to share is observed in the energetic window just below the Fermi level. Although the DOS are unambiguously greater than zero, the (p)COHP analysis in both cases predicts non-bonding interactions (i.e., $(\mathrm{p})\mathrm{COHP} \approx 0$). This would certainly warrant further investigations which are to be reported elsewhere. In summary, we see that also this class of systems is treatable with the method presented here without hassle, and the pCOHP is in complete agreement with intuitive expectations.

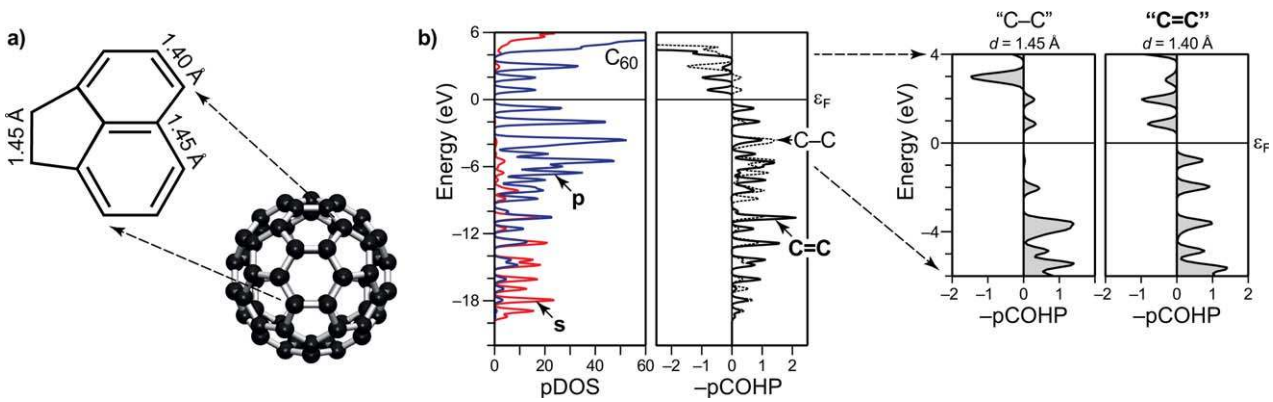

Figure 8. (a) As Figure 7b, but for an isolated entity of the carbon allotrope C_{60}. The two different bond lengths are schematically sketched and allude to idealized bond orders. (b) pDOS analysis (red curve: s-levels, blue curve: p-levels) as well as pCOHP analysis for the two bonds under study. The inset on the right is a magnified view of the pCOHP around the Fermi level. [Color figure can be viewed in the online issue, which is available at wileyonlinelibrary.com.]

What about molecules? Fullerene C_{60}

As a final example, we chose another allotrope of carbon: C_{60},[51] which, in the gas phase, is a molecule; see Figure 8a. Hence, there is no periodicity at all to consider, which is practically achieved by enlarging the simulation box around the molecule, so that no significant interactions are possible anymore. Because of the molecular character, the calculation is carried out at the Γ point only.

As already expected from the preceding carbon-based examples, the charge spilled in the C_{60} projection amounts to $\mathcal{S}_Q = 8.69\%$, and we may safely assume a reliable analysis of the electronic structure, once again. Indeed, Figure 8b shows the local DOS as separated into s- and p-contributions and reveals that all states near to the Fermi level arise from p-levels, rather typical for the π-system.

With respect to interatomic distances, two different bonds exist in the molecule, which may be naïvely regarded as "single" and "double" bonds, sketched in accordance with chemical intuition in Figure 8a. We carefully checked that this distinction is also valid for the pCOHP analysis and, hence, we show only one pCOHP curve for each kind of the bonds in Figure 8b. To further analyze the differences in the proximity of the Fermi level ε_F, the pCOHP of the longer 1.45-Å bond is magnified on the right together with the one of the shorter 1.40-Å bonds. The comparison immediately reveals that only the "double" bond appears to be fully optimized with respect to the electron count because only here all bonding states are fully occupied. In contrast, the "single" bond incorporates a nonbonding contribution just below the Fermi level and additional (but unoccupied) bonding states right above the highest occupied molecular orbital (HOMO). Upon evaluation of the energy integrals of the pCOHP, we find that the shorter "double" bond is indeed stronger (6.4 eV) than the longer "single" bond (5.9 eV), just as expected, but this is just a first (and rather rough) energetic estimate based on the bandstructure energy (i.e., the sum of the effective one-particle eigenvalues).

Conclusions

We have given expressions for projecting PW DFT eigenstates onto local orbitals of the Slater-type, and the integrals are solved analytically. The expansion to the PAW framework is derived, which makes the projection viable for state-of-the-art PW electronic-structure codes. Chemical-bonding analytic tools like the recently proposed pCOHP are reliably accessible in this framework and lend themselves to intuitive chemical interpretation. Although the minimal STO basis leads to appealing results and correctly conveys the chemical message, further optimization of the local auxiliary basis seems a rewarding target for future research. This, as well as further studies of the bonding in more complex materials, are currently underway in our laboratory.

Acknowledgments

It is a pleasure to thank the German National Academic Foundation for a scholarship to VLD. The authors thank Marc Esser for valuable discussions, and Dr. Bernhard Eck for adding support for pCOHP analysis to his visualization tool wxDragon. In addition, they also thank two perceptive reviewers for constructive criticism as regards to projection, spilling, and orthogonalization issues.

APPENDIX

To rigorously derive eq. (15), we insert the Bloch sum and the PW definition into the scalar product, given by

$$T^{\mathrm{PS}}_{\mu,j}(\vec{k}) = \langle \chi_\mu(\vec{k}) | \tilde{\psi}_j(\vec{k}) \rangle \tag{A1}$$

$$= \frac{1}{\sqrt{\Omega N_{\vec{T}}}} \sum_{\vec{G}} C^{\mathrm{PW}}_{j\vec{G}}(\vec{k}) e^{i(\vec{k}+\vec{G})\vec{R}_A} \int d^3\vec{r}\ e^{i(\vec{k}+\vec{G})\vec{r}} \sum_{\vec{T}} e^{-i\vec{k}\vec{T}} \chi_\mu(\vec{r}-\vec{T}) \tag{A2}$$

$$= \frac{1}{\sqrt{\Omega N_{\vec{T}}}} \sum_{\vec{G}} C^{\mathrm{PW}}_{j\vec{G}}(\vec{k}) e^{i(\vec{k}+\vec{G})\vec{R}_A} \sum_{\vec{T}} e^{-i\vec{k}\vec{T}} \int d^3\vec{r}\ e^{i(\vec{k}+\vec{G})\vec{r}} \chi_\mu(\vec{r}-\vec{T}). \tag{A3}$$

Now, we replace $\vec{r} = \vec{r} + \vec{T}$ and use the choice of G vectors as commonly used in PAW programs, so that $\vec{G}\cdot\vec{T} = 2\pi$:

$$T^{\mathrm{PS}}_{\mu,j}(\vec{k}) = \frac{1}{\sqrt{\Omega N_{\vec{T}}}} \sum_{\vec{G}} C^{\mathrm{PW}}_{j\vec{G}}(\vec{k}) e^{i(\vec{k}+\vec{G})\vec{R}_A} \times \underbrace{\sum_{\vec{T}} e^{-i\vec{k}\vec{T}+i(\vec{k}+\vec{G})\vec{T}}}_{=N_{\vec{T}}} \int d^3\vec{r}\ e^{i(\vec{k}+\vec{G})\vec{r}} \chi_\mu(\vec{r}) \tag{A4}$$

$$= \sqrt{\frac{N_{\vec{T}}}{\Omega}} \sum_{\vec{G}} C^{\mathrm{PW}}_{j\vec{G}}(\vec{k}) e^{i(\vec{k}+\vec{G})\vec{R}_A} \int d^3\vec{r}\ e^{i(\vec{k}+\vec{G})\vec{r}} \chi_\mu(\vec{r}). \tag{A5}$$

Then, we derive the second scalar product and remember that the functions $\bar{\phi}_\mu(\vec{r})$ are zero outside the PAW spheres around the atoms. First, we assume nonoverlapping spheres. Second, two types of overlap integrals remain: one type, where the PAW sphere and the basis function are located at the same center, which can be calculated as follows:

$$\langle \chi_\nu(\vec{k}) | \bar{\phi}_\mu(\vec{k}) \rangle = N_{\vec{T}}^{-1} \sum_{\vec{T}} \sum_{\vec{T}'} e^{i\vec{k}(\vec{T}'-\vec{T})} \int d^3\vec{r}\ \chi_\nu(\vec{r}-\vec{T}) \bar{\phi}_\mu(\vec{r}-\vec{T}') \tag{A6}$$

$$= N_{\vec{T}}^{-1} \underbrace{\sum_{\vec{T}} \sum_{\vec{T}'} \delta_{\vec{T}\vec{T}'}}_{=N_{\vec{T}}} \int d^3\vec{r}\ \chi_\nu(\vec{r}) \bar{\phi}_\mu(\vec{r}). \tag{A7}$$

By separating the three-dimensional integral into its radial and angular parts, we can make use of the orthonormality relation of the spherical harmonics and write

$$\langle \chi_\nu(\vec{k}) | \bar{\phi}_\mu(\vec{k}) \rangle = \delta_{\vec{T}\vec{T}'} \delta_{\mu\nu} \int dr\ \chi_\nu(r) \bar{\phi}_\mu(r). \tag{A8}$$

The second type appears when the two functions are centered on different atoms. As we deal with exponentially

decaying basis functions, their contribution can safely be expected to be small. Nevertheless, the integral also depends on $\bar{\phi}_\mu(\vec{r})$, which is not normalized, such that the integral is difficult to estimate in general, and the computation of these two-center integrals is nontrivial computationally. In a recent related work,[20] Dunnington and Schmidt reported a method to approximate the latter off-site integrals, which in turn formally removes the boundaries of the charge spilling (i.e., $\mathcal{S}_Q$ is no longer delimited by 0 and 1). To avoid the latter, we decided to neglect those overlaps completely. Our results show that, for the purposes of the present study (namely visual interpretation of pDOS and pCOHP contributions), this assumption is perfectly reasonable.

Keywords: chemical bonding · crystal orbital Hamilton population · density-functional theory · population analysis · projector augmented-wave method

How to cite this article: S. Maintz, V. L. Deringer, A. L. Tchougréeff, R. Dronskowski. *J. Comput. Chem.* **2013**, *34*, 2557–2567. DOI: 10.1002/jcc.23424

[1] J. Hafner, *J. Comput. Chem*. **2008**, *29*, 2044.
[2] G. Kresse, J. Furthmüller, *Comput. Mater. Sci*. **1996**, *6*, 15.
[3] R. S. Fellers, D. Barsky, F. Gygi, M. Colvin, *Chem. Phys. Lett*. **1999**, *312*, 548.
[4] (a) G. Gui, J. Li, J. Zhong, *Phys. Rev. B* **2008**, *78*, 075435; (b) G. Giovannetti, P. A. Khomyakov, G. Brocks, V. M. Karpan, J. van den Brink, P. J. Kelly, *Phys. Rev. Lett*. **2008**, *101*, 026803.
[5] V. Zólyomi, J. Kürti, *Phys. Rev. B* **2004**, *70*, 085403.
[6] A. Groß, Theoretical Surface Science: A Microscopic Perspective; Springer: Berlin, Heidelberg, **2009**.
[7] S. Tosoni, C. Tuma, J. Sauer, B. Civalleri, P. Ugliengo, *J. Chem. Phys*. **2007**, *127*, 154102.
[8] V. Hoepfner, V. L. Deringer, R. Dronskowski, *J. Phys. Chem. A* **2012**, *116*, 4551.
[9] T. Hughbanks, R. Hoffmann, *J. Am. Chem. Soc*. **1983**, *105*, 3528.
[10] R. Hoffmann, Solids and Surfaces. A Chemist's View of Bonding in Extended Structures; VCH Publishers Inc.: New York, **1988**.
[11] R. Dronskowski, P. E. Blöchl, *J. Phys. Chem*. **1993**, *97*, 8617.
[12] R. Dronskowski, Computational Chemistry of Solid State Materials; Wiley-VCH: Weinheim, New York, **2005**.
[13] (a) V. Svitlyk, G. J. Miller, Y. Mozharivskyj, *J. Am. Chem. Soc*. **2009**, *131*, 2367; (b) J.-C. Dai, S. Gupta, O. Gourdon, H.-J. Kim, J. D. Corbett, *J. Am. Chem. Soc*. **2009**, *131*, 8677; (c) J. Brgoch, C. Goerens, B. P. T. Fokwa, G. J. Miller, *J. Am. Chem. Soc*. **2011**, *133*, 6832; (d) S. B. Schneider, R. Frankovsky, W. Schnick, *Inorg. Chem*. **2012**, *51*, 2366.
[14] D. J. Chadi, *Phys. Rev. B* **1977**, *16*, 3572.
[15] D. Sánchez-Portal, E. Artacho, J. M. Soler, *Solid State Commun*. **1995**, *95*, 685.
[16] D. Sánchez-Portal, E. Artacho, J. M. Soler, *J. Phys. Condens. Matter* **1996**, *8*, 3859.
[17] M. D. Segall, C. J. Pickard, R. Shah, M. C. Payne, *Mol. Phys*. **1996**, *89*, 571.
[18] M. D. Segall, R. Shah, C. J. Pickard, M. C. Payne, *Phys. Rev. B* **1996**, *54*, 16317.
[19] N. Börnsen, B. Meyer, O. Grotheer, M. Fähnle, *J. Phys. Condens. Matter* **1999**, *11*, L287.
[20] B. D. Dunnington, J. R. Schmidt, *J. Chem. Theory Comput*. **2012**, *8*, 1902.
[21] V. L. Deringer, A. L. Tchougréeff, R. Dronskowski, *J. Phys. Chem. A* **2011**, *115*, 5461.
[22] I. Bako, A. Stirling, A. P. Seitsonen, I. Mayer, *Chem. Phys. Lett*. **2013**, *563*, 97.
[23] L. P. Lee, D. J. Cole, M. C. Payne, C.-K. Skylaris, *J. Comput. Chem*. **2013**, *34*, 429.
[24] T. R. Galeev, B. D. Dunnington, J. R. Schmidt, A. I. Boldyrev, *Phys. Chem. Chem. Phys*. **2013**, *15*, 5022.
[25] M. Chen, U. V. Waghmare, C. M. Friend, E. Kaxiras, *J. Chem. Phys*. **1998**, *109*, 6854.
[26] P. E. Blöchl, *Phys. Rev. B* **1994**, *50*, 17953.
[27] G. Kresse, D. Joubert, *Phys. Rev. B* **1999**, *59*, 1758.
[28] F. Bloch, *Z. Phys*. **1929**, *52*, 555.
[29] C. Bunge, J. Barrientos, A. Bunge, *At. Data Nucl. Data Tables* **1993**, *53*, 113.
[30] T. Koga, K. Kanayama, S. Watanabe, A. J. Thakkar, *Int. J. Quantum Chem*. **1999**, *71*, 491.
[31] T. Koga, K. Kanayama, T. Watanabe, T. Imai, A. J. Thakkar, *Theor. Chem. Acc*. **2000**, *104*, 411.
[32] D. Belkič, H. S. Taylor, *Phys. Scr*. **1989**, *39*, 226.
[33] P. Löwdin, *J. Chem. Phys*. **1950**, *18*, 365.
[34] G. Kresse, J. Hafner, *Phys. Rev. B* **1993**, *47*, 558.
[35] G. Kresse, J. Furthmüller, *Phys. Rev. B* **1996**, *54*, 11169.
[36] J. P. Perdew, K. Burke, M. Ernzerhof, *Phys. Rev. Lett*. **1996**, *77*, 3865.
[37] O. Jepsen, O. K. Andersen, *Solid State Commun*. **1971**, *9*, 1763.
[38] P. E. Blöchl, O. Jepsen, O. K. Andersen, *Phys. Rev. B* **1994**, *49*, 16223.
[39] H. J. Monkhorst, J. D. Pack, *Phys. Rev. B* **1976**, *13*, 5188.
[40] B. Eck, wxDragon 1.8.7, 2013. Available at http://www.wxdragon.de.
[41] O. K. Andersen, *Phys. Rev. B* **1975**, *12*, 3060.
[42] O. K. Andersen, O. Jepsen, *Phys. Rev. Lett*. **1984**, *53*, 2571.
[43] J. P. Perdew, Y. Wang, *Phys. Rev. B* **1992**, *45*, 13244.
[44] S. H. Vosko, L. Wilk, M. Nusair, *Can. J. Phys*. **1980**, *58*, 1200.
[45] G. Markopoulos, P. Kroll, R. Hoffmann, *J. Am. Chem. Soc*. **2010**, *132*, 748.
[46] G. A. Landrum, R. Dronskowski, *Angew. Chem. Int. Ed.*. **2000**, *39*, 1560.
[47] R. Dovesi, R. Orlando, B. Civalleri, C. Roetti, V. R. Saunders, C. M. Zicovich-Wilson, *Z. Kristallogr*. **2005**, *220*, 571.
[48] J. M. Soler, E. Artacho, J. D. Gale, A. García, J. Junquera, P. Ordejón, D. Sánchez-Portal, *J. Phys. Condens. Matter* **2002**, *14*, 2745.
[49] H. Choi, R. C. Longo, M. Huang, J. N. Randall, R. M. Wallace, K. Cho, *Nanotechnology* **2013**, *24*, 105201.
[50] R. Hoffmann, *Angew. Chem. Int. Ed.* **2013**, *52*, 93.
[51] H. W. Kroto, J. R. Heath, S. C. O'Brien, R. F. Curl, R. E. Smalley, *Nature* **1985**, *318*, 162.

Received: 10 June 2013
Revised: 30 July 2013
Accepted: 7 August 2013
Published online on 10 September 2013